# Additive manufacturing of functionally graded transition joints between ferritic and austenitic alloys

J.S. Zuback [a], T.A. Palmer [a, b], T. DebRoy [a, *]

[a] *Department of Materials Science and Engineering, The Pennsylvania State University, University Park, PA, 16802, USA*
[b] *Department of Engineering Science and Mechanics, The Pennsylvania State University, University Park, PA, 16802, USA*

### A B S T R A C T

Dissimilar metal joints between ferritic and austenitic alloys are susceptible to premature failure due to diffusive carbon loss from the ferritic alloy driven by abrupt changes in carbon chemical potential. Compositional grading of transition joints fabricated using laser-based directed energy deposition additive manufacturing offers a means for limiting carbon diffusion. Here we fabricate functionally graded transition joints between a ferritic and austenitic alloy, characterize spatial variations of chemical composition, microstructure and hardness, and test their effectiveness to limit carbon loss from the ferritic alloy. Microstructural studies and carbon potential variations in the functionally graded material showed that the length of the joints can be shorter, and there is no benefit to continue compositional grading once the microstructure becomes fully austenitic. Since dissimilar joints have an expected lifetime of several decades, long service times were simulated through accelerated heat treatment experiments at elevated temperatures for both a dissimilar metal weld and a functionally graded transition joint. While the dissimilar weld showed pronounced carbon loss from the ferritic side, there was insignificant change in the carbon concentration profile in the functionally graded joint indicating effectiveness of the graded joints to perform under service conditions.

© 2018 Elsevier B.V. All rights reserved.

## 1. Introduction

Dissimilar metal joints between ferritic and austenitic materials are commonly used in applications such as superheater tubes and vessel to piping welds of nuclear energy generation facilities [1–4]. Ferritic low-alloy steels are often used in pressure vessels due to their good strength and corrosion resistance at elevated service temperatures. Austenitic stainless steels and Fe-Ni-Cr alloys offer excellent high temperature strength, resistance to oxidation, and creep rupture properties. Fusion welding between these dissimilar materials is typically performed with a nickel-based filler metal to alleviate problems due to the mismatch in the coefficient of thermal expansion (CTE). However, abrupt changes in chemical composition, microstructure, and mechanical properties are observed [2,4–6], leading to a degradation in the performance of the joint during long-term high temperature service [1].

Of all contributing factors, carbon diffusion from ferritic to austenitic alloys has been identified as a major cause for premature

failure of dissimilar metal joints [2,4,7]. Although nuclear power plants are designed to last for several decades, after just one to two decades of service, a band of carbides is typically found on the austenitic side of the interface [4] due to carbon accumulation driven by the spatial gradient of the carbon chemical potential. The large carbon solubility of the austenite phase and presence of carbide forming elements, such as chromium, create a driving force for carbon diffusion away from the ferritic steel [8,9]. Consequently, a soft, carbon-depleted zone forms along the interface in the ferritic steel, leading to premature failures of the joints near the fusion line [4,10,11]. Current practices of joining ferritic steels to austenitic stainless steels introduce an intermediate austenitic alloy welded to the ferritic steel using Ni-base filler metals [2–4]. Although this method has been shown to reduce the CTE mismatch and increase service life, the problem of carbon diffusion remains unsolved.

Functionally graded materials (FGMs) are a method of joining ferritic and austenitic materials that can reduce the driving force for carbon diffusion and improve performance of the joints. FGMs are defined as a class of materials with spatially variable properties tailored to achieve a specific function [12]. Variations in geometry, density, composition, or microstructure are typically designed at

* Corresponding author.
*E-mail address:* debroy@psu.edu (T. DebRoy).

specific locations in FGMs to enhance mechanical properties [13], improve service performance [14], or increase compatibility with other systems [15]. A common example of FGMs is also found in orthopedic implants, which are designed with gradients in porosity to allow for bone growth while providing load-bearing support [16]. In FGMs, the chemical composition can be spatially varied to eliminate the abruptness of carbon chemical potential variation, thus mitigating the diffusive carbon loss from the ferritic alloy at elevated service temperatures.

Additive manufacturing (AM) technologies offer an attractive way for producing FGMs in which the chemical composition [17,18], part density [19], and process parameters [20] can be tailored to achieve the desired microstructure and properties with good spatial resolution. Laser-based directed energy deposition (DED) using powder feedstock is a commonly used method for tailoring composition gradients by controlling the powder flow rates of different alloy powders into the molten pool [21,22]. For example, composition gradients between Ti-6Al-4V and pure V [21], Inconel® (IN) 625 and 304L and 316 stainless steel (SS) [18,23], pure Fe and Fe-50 at% Al [24], SS 316L and Stellite 6 [25], Ti-6Al-4V and IN 718 [26] and Invar [27], and Ti and Ti-Mo/V [28] have been fabricated. Even if care is taken in producing smooth compositional transitions, secondary phases, like intermetallic compounds and carbides, are shown to form at specific compositions [18,22,27] and they often affect the service performance of the components.

Here we seek to reduce carbon diffusion between dissimilar ferritic and austenitic alloys by fabricating FGMs between 2.25Cr-1Mo steel and Alloy 800H using additive manufacturing. While a smooth, gradual change in chemical composition was anticipated, the spatial variations of microstructure, chemical composition and hardness were examined at various locations in the graded joint. Since the dissimilar metal joints are subjected to elevated temperatures for decades during service, the effectiveness of the graded joints to retard carbon transport was tested by designing and conducting accelerated heat treatment experiments to simulate the service conditions. We present experimental data to establish that unlike the dissimilar welds, there was no significant change in the carbon concentration profile in the compositionally graded joint resulting from the simulated service conditions.

## 2. Materials and methods

A laser-based DED process was used to fabricate a series of compositionally graded joints on a normalized and tempered 150 mm × 150 mm x 12.7 mm thick SAE387 Grade 22 steel substrate. A ytterbium fiber laser (IPG Photonics® YLR-12000-L) with a wavelength ranging from 1070 to 1080 nm was used at a power of 2000 W and a travel speed of 10.6 mm/s, giving a linear heat input of 189 J/mm. Powder was delivered through four nozzles with 1.6 mm diameter orifices at a total flow rate of approximately 0.25 g/s. Each nozzle was angled to converge the powder streams coaxially with the laser to a spot 10 mm below the point of exit, which corresponds to a laser beam radius of approximately 2 mm. During processing, the build chamber was purged with high purity argon, and the oxygen content was held between 300 and 500 ppm to reduce the potential for oxidation of the deposited material [29,30].

Compositional grading was achieved by blending Pyromet® 800 (800H) and the custom blended Fe-Cr mixture (Fe-2.25Cr) to produce the desired composition prior to deposition at each height of the gradient. A total of 9 different mixtures from 10% to 90% 800H were blended in increments of 10% 800H using a twin screw mixing method. The powder feedstock used during deposition consisted of pre-alloyed Pyromet® 800 (Carpenter Powder Products, Inc.) and commercially pure iron and chromium (Atlantic Equipment

Engineers, Micron Metals, Inc.). All powders had a size range from 45 to 145 μm in diameter, and compositions of the substrate and powders are shown in Table 1. The laser beam remained off for approximately 5 min each time that a new powder mixture was switched. While this method added to the overall machine time, discontinuous processes have been shown to be beneficial for reducing residual stresses and distortion [31]. A total of 34 layers were deposited using 5 passes per layer during a total processing time of approximately 1 hr. All passes within a layer were scanned in the same direction, and successive layers were scanned in the opposite direction to produce an alternating layer build path plan.

After deposition, a thin slice was extracted near the middle of the deposit using electrical discharge machining to reveal the transverse cross section. The sample was mounted and ground with a series of silicon carbide papers up to P2000 ISO grit size, polished with 3 μm and 1 μm polycrystalline diamond suspension, and finished with 0.05 μm colloidal silica. The cross section was etched by immersion for approximately 2 s with Marble's reagent, which is a solution of 20 g of copper sulfate ($CuSO_4$), 100 mL of hydrochloric acid (HCl), and 100 mL distilled water ($H_2O$) to reveal grain boundaries as well as sub-grain structures. Scanning electron microscopy (SEM) using an FEI Quanta 200 was used to examine microstructures along the composition gradient. A 20 kV accelerating voltage was used for both secondary electron and backscatter electron images.

Micro-hardness measurements were taken using a LECO M-400-G1 microhardness tester with a Vickers indenter. A 300 g load with a dwell time of 5 s was used for all indentations. Hardness traces were recorded at 1 mm intervals along the build direction starting at the fusion line between the base metal and the first layer of the deposition. This spacing was chosen to coincide with the approximate layer height of 1 mm and to avoid interactions between individual hardness indents. A total of 5 measurements were taken per layer at each height.

Local values of chemical composition along the grading direction were measured by electron probe microanalysis (EPMA) using a CAMECA SXFive probe. The instrument was operated at a voltage of 20 keV and current of 30 nA. The EPMA trace spanned vertically along the build direction in increments of 1 mm and the main alloying elements (Fe, Ni and Cr) in the graded joint were analyzed.

To study carbon diffusion, a dissimilar metal weld (DMW) and the FGM were heat treated at 725 °C for 235 h and subsequently air-cooled. The DMW consisted of 2.25Cr-1Mo steel joined to Alloy 800H using IN82 filler metal by a multi-pass gas metal arc welding process. Carbon concentrations before and after heat treatment were measured using EPMA with a 15 kV accelerating voltage and 200 nA beam current. A liquid nitrogen cooling trap kept at approximately −190 °C was used to limit contamination. A total of three line scans measuring 300 μm each were centered on the interface of interest in 1 μm steps using a 5 s counting time at each location and the number of counts per second were recorded in each sample. The number of counts per second were converted to wt% C by calibrating the known carbon concentrations of NIST standard reference materials containing 0.016 wt% C (SRM2159), 0.1143 wt% C (SRM36b) and 0.082 wt% C (SRM866) through linear interpolation.

Computational thermodynamic and kinetic calculations were performed by implementing the CALPHAD technique [32]. Using chemical composition as input, carbon chemical potentials and martensite transformation temperatures for various regions of the FGM were calculated using the General Steel database of the software JMatPro® V8 (Sente Software LTD, United Kingdom). The carbon concentration profiles after simulated service conditions were calculated using the TCFE8 and MOBFE3 databases of ThermoCalc® and DICTRA® (Thermocalc Software AB, Stockholm,

**Table 1**
Chemical compositions of substrate and powder used for deposition.

| Material | Wt% of element | | | | | | | |
|---|---|---|---|---|---|---|---|---|
| | Cr | Fe | Mn | Mo | Ni | Si | C | Other |
| Baseplate | 2.00—2.25 | Bal. | 0.30—0.60 | 0.90—1.1 | — | 0.50 | 0.05—0.15 | 0.035P, 0.035S |
| Pyromet® 800 | 21.0 | Bal. | 0.88 | — | 34.0 | 0.62 | 0.095 | 0.38Al, 0.41Ti, 0.015O |
| Fe | — | Bal. | — | — | — | — | 0.005 | 0.016S |
| Cr | Bal. | 0.07 | — | — | — | <0.01 | 0.004 | 0.43O, 0.023S |

Sweden), respectively.

## 3. Results and discussion

### 3.1. Compositional variation in the additively manufactured graded joints

Although the carbon contents in 2.25Cr-1Mo steel and Alloy 800H are roughly equal, a large thermodynamic driving force for

carbon diffusion exists due to the spatial variation of other alloying elements. Fig. 1(a) shows the carbon chemical potential variation as a function of distance at a typical service temperature of 773 K for an idealized DMW between 2.25Cr-1Mo steel and Alloy 800H using IN82 filler metal. Even when accounting for a small region of dilution roughly 40 μm in width in which alloying elements vary linearly, there is a steep change in the carbon chemical potential resulting in a large thermodynamic driving force for carbon diffusion. In contrast, Fig. 1(b) shows a gradual change in the carbon chemical potential for a FGM with a linear change in the nominal chemical compositions from 2.25Cr-1Mo steel to Alloy 800H over a distance typical of DED builds. It is evident in Fig. 1 that the thermodynamic driving force for carbon diffusion is drastically reduced in a FGM compared to a DMW.

From Fig. 1, it is clear that the control of the variation of chemical composition within the graded joint is important to reduce the driving force for carbon diffusion. Fig. 2 shows the concentrations of the main alloying elements, Fe, Ni and Cr, at various locations along the length of the AM build measured using EPMA. The expected compositions are overlaid by solid lines on the measured values for comparison. Overall, the measured compositions closely follow the expected step-wise trend of the chemical compositions. It is observed that the small deviations, particularly in the Fe concentration, occurred in regions corresponding to the interface between two layers of different compositions, which is likely due to dilution resulting from the remelting of the previously deposited layers.

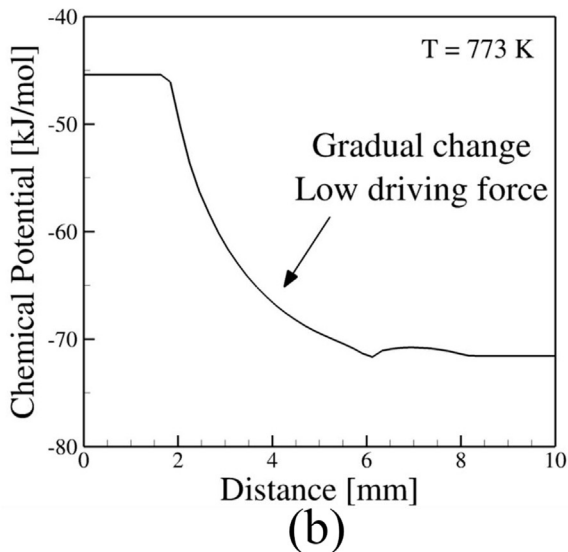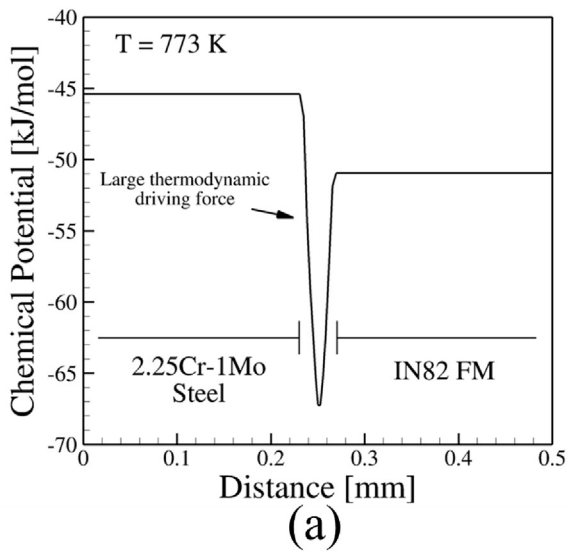Using the measured chemical compositions, the spatial



**Fig. 1.** Calculated spatial variation in carbon chemical potential for (a) a DMW and (b) a FGM between 2.25Cr-1Mo steel and Alloy 800H.
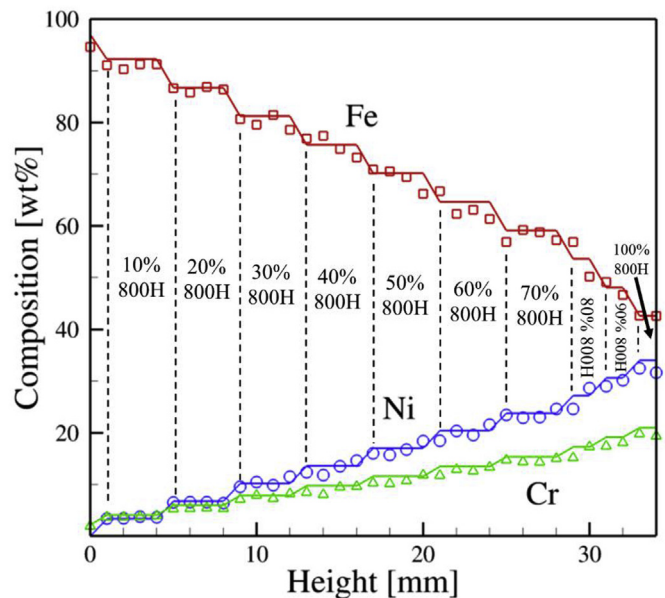


**Fig. 2.** Expected (solid lines) and measured (symbols) chemical composition along the build height.

variation of the carbon chemical potential can be calculated at any given temperature. Fig. 3 shows the chemical potential of carbon as a function of distance along the length of the functionally graded joint at a typical service temperature of 773 K. Compared to DMWs, the change in the carbon chemical potential in the FGM is gradual and no abrupt changes in chemical potential occurs, thus significantly reducing the driving force for carbon diffusion from the ferritic steel to the austenitic alloy.

### 3.2. Spatial variation of microstructure and hardness

Parts fabricated by laser-based DED are subjected to complex thermal cycles during deposition. These thermal cycles and the spatial variation of the chemical composition lead to local changes in both microstructure and properties within the graded joints. In order to understand the phases present in various regions, the microstructure and the measured hardness values were examined together with the Schaeffler diagram, which is commonly used for determining the main microstructural phases formed during fusion welding of alloy steels, stainless steels, and DMWs [33,34]. Fig. 4 shows Vickers hardness traces measured along the height of the build. Regions of martensite and austenite predicted by the Schaeffler diagram (Fig. 5) are shown by the dotted lines. The measured compositions (in wt%) at each location were converted to nickel and chromium equivalents, as defined in equations (1) and (2),

$$Ni_{EQ} = \%Ni + 30*\%C + 0.5*\%Mn \tag{1}$$

$$Cr_{EQ} = \%Cr + \%Mo + 1.5*\%Si + 0.5*\%Nb \tag{2}$$

Significant differences in Vickers hardness are observed as a function of build height. The highest hardness values fall within the fully martensitic region, and some scatter in the hardness measurements are observed in the region containing a combination of martensite and austenite due to hardness differences of the two phases. The lowest Vickers hardness measurements were recorded in the fully austenitic regions.

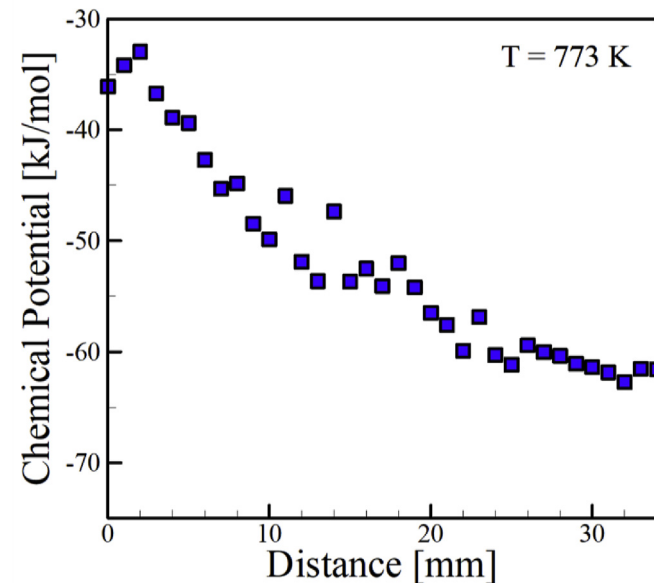From the middle to the top of the build, at a heights of 17 mm
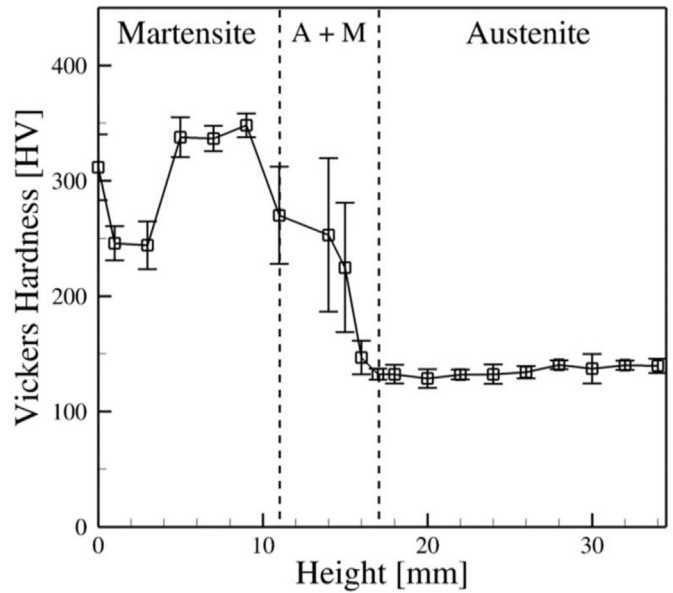


**Fig. 4.** Vickers hardness measurements along the functionally graded sample. Regions of martensite, austenite and a mixture of austenite and martensite predicted by the Schaeffler diagram are separated by dashed lines.
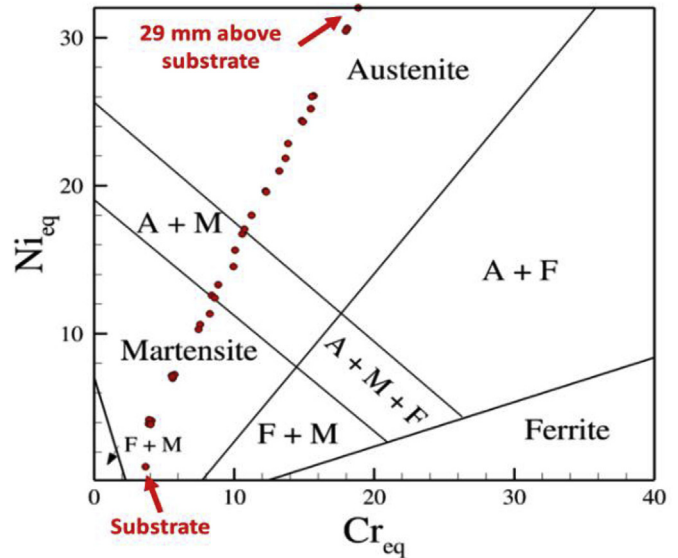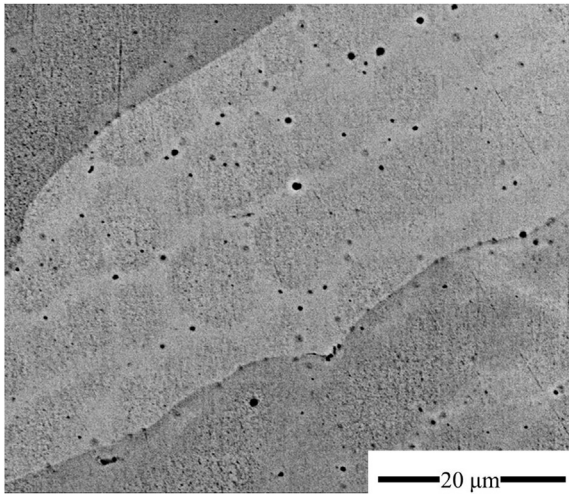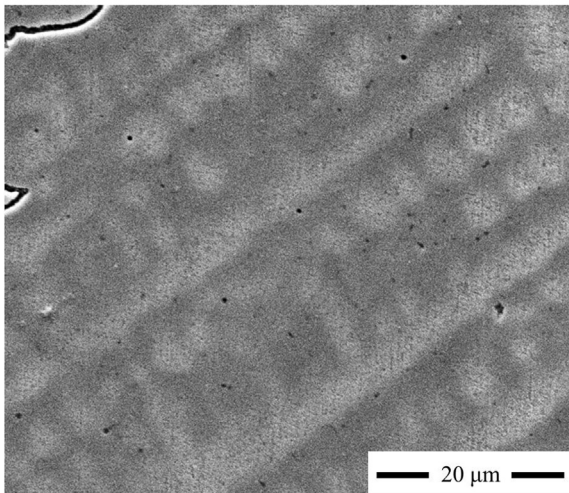


**Fig. 5.** Nickel and chromium equivalents converted from the measured chemical composition plotted on the Schaeffler diagram.

and above from the plate, the compositions correspond to powder blends from 50 to 100% 800H with approximate $Cr_{EQ}$ values ranging from 8.4 to 21 and $Ni_{EQ}$ values ranging from 12.6 to 35. A plateau in Vickers hardness was reached in this region and measurements showed a consistent value slightly below 150 HV and a columnar dendritic microstructure was present, as displayed in Fig. 6a and b. The microstructure displayed large, elongated grains of austenite with a dendritic sub-structure.

In the regions slightly below the middle of the build, the measured Vickers hardness values were higher than the values observed in the fully austenitic region above. The higher hardness values are consistent with the appearance of martensite of various compositions. Fig. 7(a) and (b) show SEM micrographs at (a) 11 mm
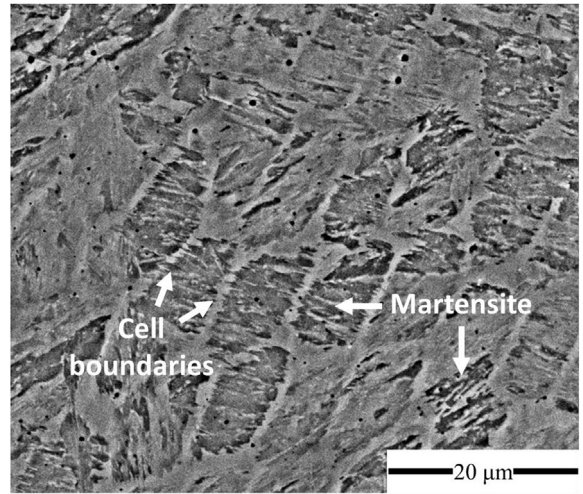


**Fig. 3.** Calculated carbon potential as a function of distance at 773 K (500 °C) and atmospheric pressure for the measured compositions shown in Fig. 2.
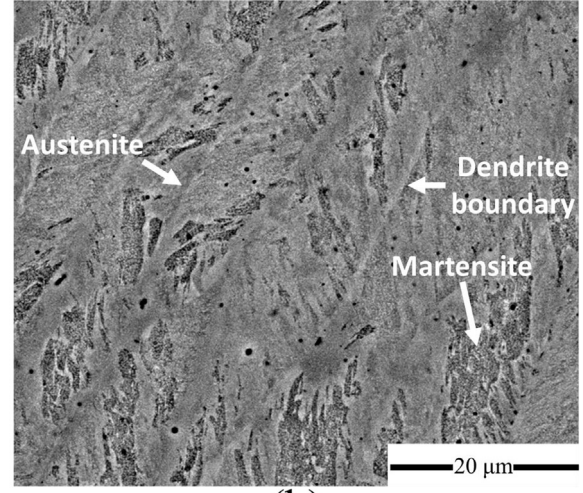
**Fig. 6.** SEM micrographs approximately (a) 19 mm and (b) 34 mm from the baseplate in the build direction. The microstructures correspond to the 19th and 34th deposited layer, and compositions of 50 and 100% 800H, respectively.

**Fig. 7.** SEM micrographs approximately (a) 11 mm and (b) 15 mm from the baseplate in the build direction. The microstructures correspond to the 11th and 15th deposited layers and compositions of 30 and 40% 800H, respectively.

and (b) 15 mm from the baseplate in the build direction. Sharp martensitic laths and larger austenitic blocks are present at each location. These microstructures correspond to the 11th and 15th deposited layers and compositions of 30 and 40% 800H, respectively. The hardness values displayed somewhat larger scatter in this two phase austenite and martensite region. The large standard deviations of hardness indicate microstructural inhomogeneities consisting of hard martensitic regions dispersed in a softer austenite matrix.

To explain the varying amounts of austenite and martensite in the two phase region, it is worthwhile to investigate the martensite transformation temperatures. Fig. 8 shows calculations of martensite start temperature, $M_s$, 50% completion temperature, $M_{50}$, and finish temperature, $M_f$, as a function of 800H additions. The $M_s$ temperature is the temperature at which the free energy difference between the austenite and ferrite phases reaches a critical value for martensite nucleation [35]. At additions up to 30% 800H, both $M_s$ and $M_f$ are above room temperature, meaning that the martensitic transformation is likely to reach completion. At a composition of 40% 800H, $M_f$ drops below room temperature,

indicating that although the transformation has started, it does not reach completion upon cooling to room temperature and some amounts of austenite are retained. After 40% 800H, the calculations show that the $M_s$ values drops below room temperature, prohibiting the martensitic transformation from ever initiating, leading to high amounts of austenite.

Closer to the base plate, a much harder martensitic region is observed in the microstructure with a HV of 350 at a location 7 mm above the base. Fig. 9(a) shows the microstructure present at a location 7 mm above the baseplate corresponding to a composition of 20% 800H. The solidification sub-grain structure of dendrite boundaries are easily observable, as further shown at higher magnification in Fig. 9(b) and displays large amounts of lath martensite. Smaller regions of austenite appear as indicated by the white arrows.

Within the first 4 mm of the build height, the hardness drops to a level of approximately $245 \pm 15$ HV. The composition in this region corresponds to a powder blend representing 10% 800H and $Ni_{EQ}$ and $Cr_{EQ}$ both approximately equal to 4, which is predicted by the Schaeffler diagram to be martensitic. Fig. 10 shows a micrograph in the region approximately 3 mm above the baseplate.
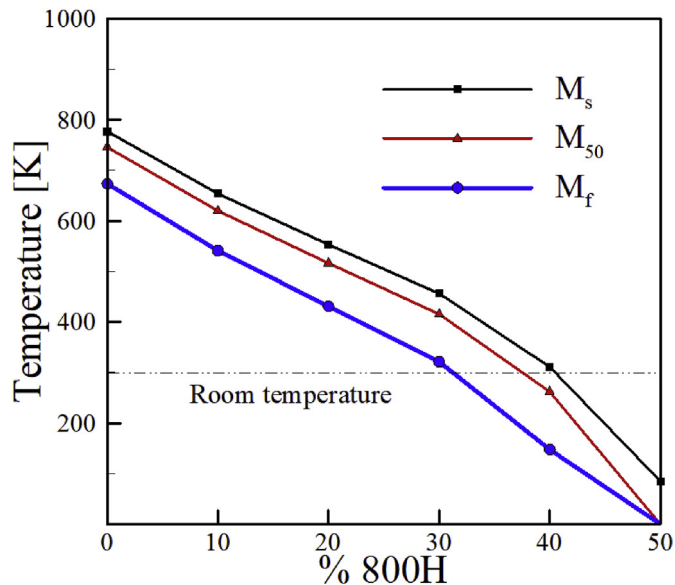
**Fig. 8.** Martensite start (M_s), 50% completion (M_50) and finish (M_f) temperatures for the martensite transformation as a function of composition in terms of percent 800H.

While no observable grain boundaries were revealed after etching, small, plate-like structures with sharp edges were present throughout the region. This type of microstructure and corresponding hardness values are consistent with the fine-grained heat affected zone commonly observed in regions of multi-pass dissimilar welds [36], where subsequent passes reheat the material to just above the austenization temperature. While the microstructure in this region is transformed to austenite, no significant grain growth occurs and the final ferritic grains remain very fine, usually on the order of tens of microns [37]. Mukherjee et al. [38] showed computationally that the peak temperature in the first layer during deposition of a second layer in a compositionally graded alloy easily reaches a value higher than the austenization temperature of this region (~760 °C).

### 3.3. Reduced carbon diffusion through the graded joints during service

The dissimilar metal welds in nuclear plants are deployed in service at about 773 K (500 °C) for several decades before their performance is compromised due to metallurgical degradation resulting from carbon migration away from the ferritic side of the joint. In order to examine the effectiveness of the FGM to overcome this problem, both the FGM and a DMW were subjected to an accelerated heat treatment to investigate carbon diffusion from the ferritic side of the joint.

Decades of typical service conditions were simulated by selecting a temperature of heat treatment that was much higher than the typical service temperature of 773 K. The selection of time and temperature was based on the application of the Larson-Miller parameter,

$$L = T(C + \log(t)) \qquad (3)$$

where $T$ is temperature in K, $C$ is a material constant, and $t$ is the time in hours. The Larson-Miller parameter is frequently used for extrapolating experimentally measured creep data for homogeneous materials to prolonged times at which laboratory experiments are not feasible. A value for $C = 20$ was chosen which
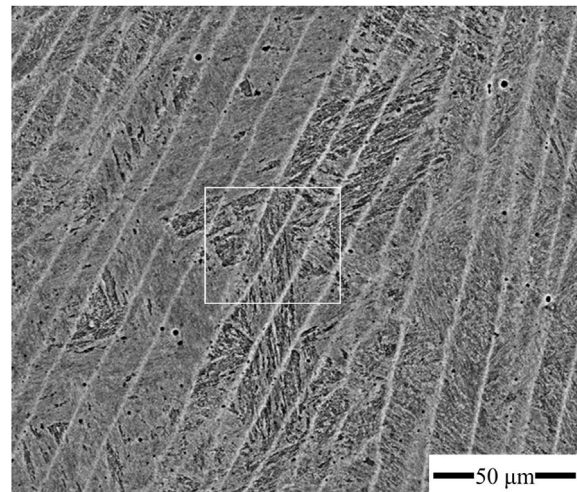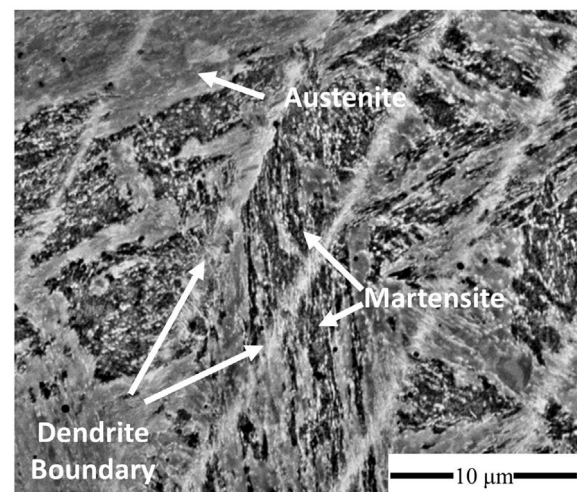




**Fig. 9.** (a) SEM micrograph approximately 7 mm from the baseplate in the build direction, corresponding to the 7th deposited layer and a composition of 20% 800H and (b) a higher magnification image outlined by the white box in (a) showing martensite and austenite.

corresponds to commonly used values for applications involving 2.25Cr-1Mo steel [39]. The DMW and FGM were held at 998 K for 235 h (~10 days). From equation (3), this treatment has an equivalent $L$ to conditions of 773 K and approximately $7.6 \times 10^8$ h.

The carbon concentration profiles measured using EPMA both before and after the accelerated heat treatments are shown in Figs. 11 and 12 for the DMW and FGM, respectively. The points for each location correspond to the average values of the three line scans and the error bars represent the standard deviation. A comparison of Fig. 11(a) and (b) show the changes in the carbon concentration profiles of the DMW before and after heat treatment, respectively. The higher concentration of carbon close to the austenitic side of the joint in Fig. 11(b) indicates carbon diffusion from ferritic to austenitic region. In contrast, when the carbon concentration profiles of the FGM specimen before and after the accelerated heat treatments are examined (Fig. 12(a) and (b)), there was only a small amount of carbon accumulation observed on the austenite side. This indicates only an insignificant amount of carbon loss from the ferritic steel after enduring service conditions that
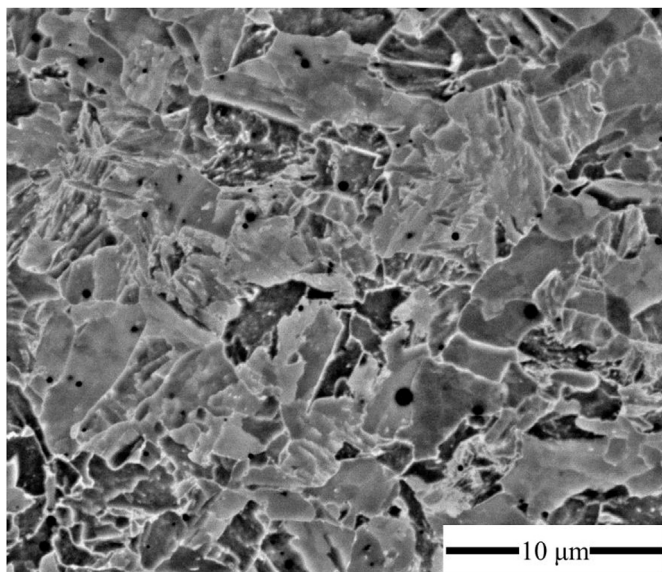
**Fig. 10.** SEM micrograph approximately 3 mm from the baseplate in the build direction, corresponding to the 3rd deposited layer and a composition of 10% 800H.

represent orders of magnitude longer times than required.

### 3.4. Predicting the observed reduction of carbon diffusion

The accelerated heat treatment and the subsequent carbon concentration profile measurements by EPMA show experimentally the ability of the compositionally graded joints to prevent the diffusive carbon loss from the ferritic side of the joint and avoid the adverse consequences of such loss. However, these experiments are time consuming and expensive. Furthermore, determination of concentration profiles of carbon by EPMA at low carbon concentrations suffer from large scatters. If a simulation tool can be relied upon to predict the outcome before the accelerated diffusion experiments, an improved anticipation can be developed and in some cases the lengthy experiments can be avoided.

To examine the reliability of the computational tools, the carbon concentration profiles in the accelerated carbon diffusion experiments were simulated. Figs. 11(b) and 12 (b) show comparison between the experimentally measured carbon concentration profiles from EPMA with the results of the simulations shown as solid lines for the DMW and FGM, respectively. The computed values agree well with the experimentally measured values of concentrations. In view of the reported difficulties of carbon concentration profile measurements for low carbon concentrations and the ability of the simulations to accurately predict the concentration profiles for both DMWs and FMGs, the simulations can be used with confidence for examining the diffusion of carbon under service conditions.

Furthermore, it was shown in Fig. 1(b) and experimentally in Fig. 3 that the carbon chemical potential roughly approaches a plateau after the 70% 800H region, meaning that further grading in chemical composition negligibly affects the driving force for carbon diffusion. Additionally, the microstructure in this region was observed to be fully austenitic and changes in chemical composition had little effect on the microhardness. Therefore, a full composition gradient from the ferritic to the austenitic alloy may not be necessary to achieve the intended function.

A metric for comparing different joint designs is through the carbon diffusion flux and resulting carbon depletion in the ferritic
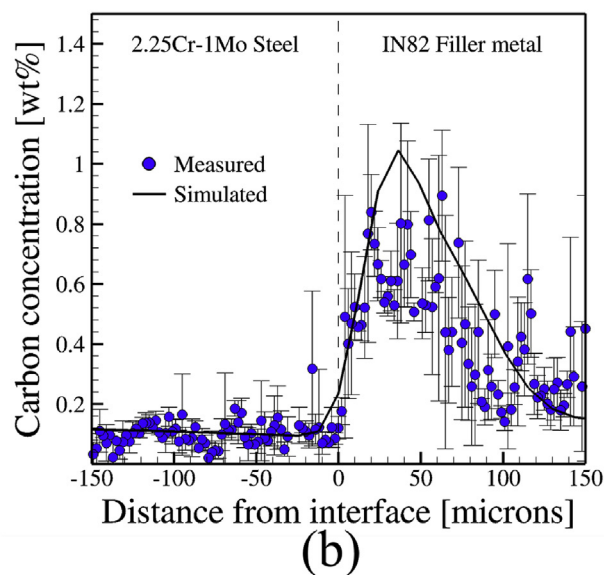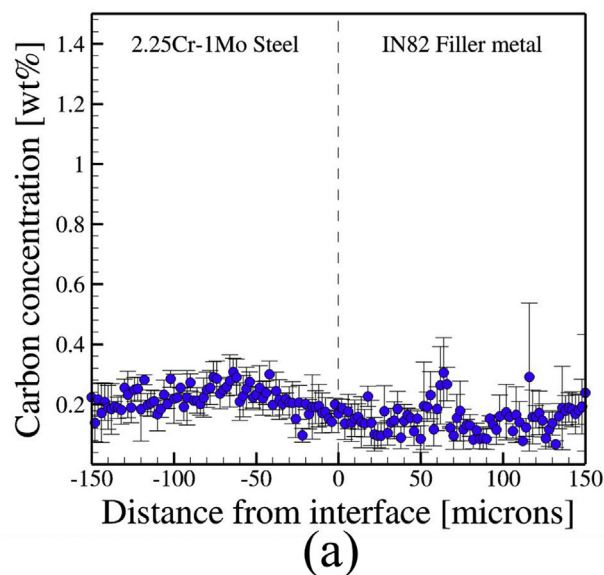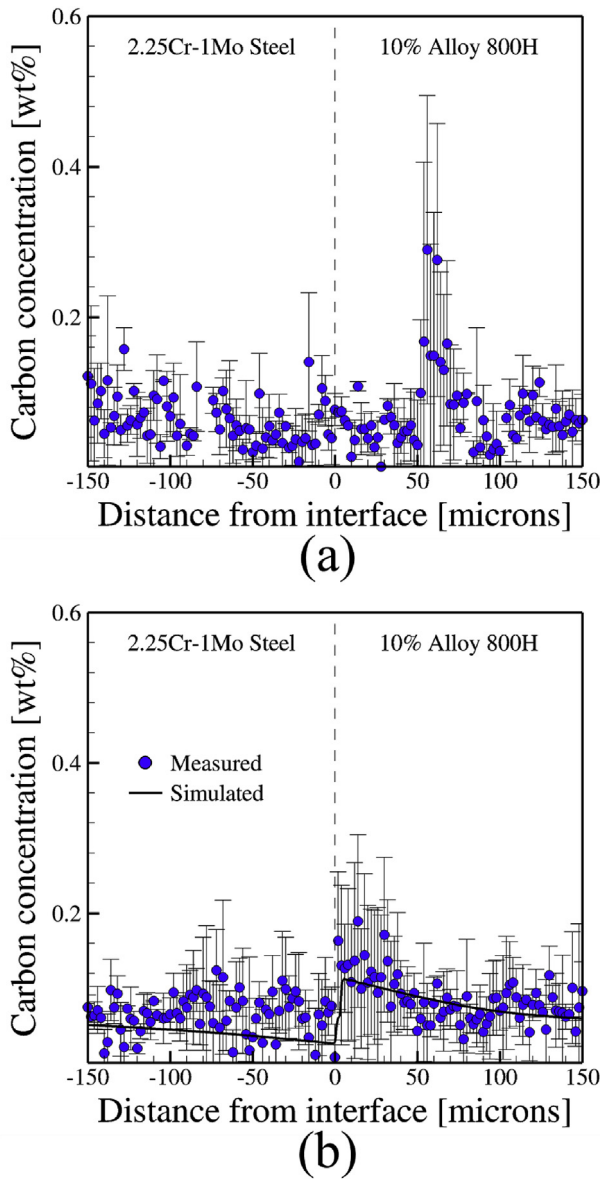




**Fig. 11.** Measured carbon concentration profiles for a DMW between 2.25Cr-1Mo steel and Alloy 800H using IN82 filler metal (a) in the as-welded condition and (b) after heat treatment.

steel. The carbon diffusion flux is a measure of the amount of carbon migrating through a unit area per unit time and is dependent on both location and time. Table 2 provides the carbon diffusion fluxes in the ferritic steel after different service times at 773 K for various joints. The calculations take into account the change in driving force with time as the system moves towards equilibrium.

In both the full and partial FGM, approximately 100 years of service are required to reach the same maximum carbon depletion as a DMW in just 5 years. No differences in maximum diffusion flux occur when comparing a full compositional grading to a FGM graded from 10 to 70% 800H because the chemical potential does not change significantly with distance for the chemical compositions considered. In terms of microstructure, no advantages can be gained in slowing carbon diffusion once the microstructure becomes fully austenitic, allowing for a shorter joint to suffice. Therefore, a FGM from 10 to 70% 800H is effective for limiting carbon diffusion and provides a shorter joint design compared to a full composition gradient.

**Fig. 12.** Measured carbon concentration profiles for a FGM between 2.25Cr-1Mo steel and Alloy 800H (a) in the as-deposited condition and (b) after heat treatment.
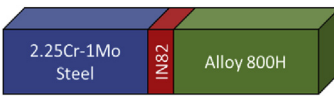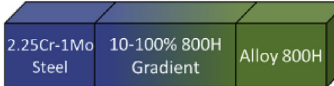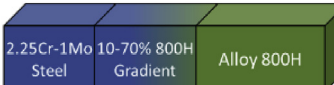
## 4. Summary and conclusions

Compositional grading of transition joints was examined as a means for limiting harmful carbon diffusion commonly encountered in dissimilar metal welds between 2.25Cr-1Mo steel and Alloy 800H. Compositional gradients were fabricated by laser-based directed energy deposition and the spatial variations of microstructure, chemical composition, and hardness were characterized. Accelerated heat treatments of both the functionally graded joints and dissimilar welds were conducted to test their effectiveness of preventing diffusive carbon loss from the ferritic alloy under service conditions. Numerical simulations of carbon diffusion during accelerated heat treatment as well as the carbon diffusion under service condition for various joint designs were undertaken. The following are the main findings.

(a) The carbon chemical potential gradient as well as the carbon diffusion rate is significantly diminished by replacing the dissimilar joints with the compositionally graded joints. It takes approximately 5 years to deplete 5% of the initial carbon in a dissimilar weld under typical service conditions. However, in an appropriately graded joint, it would take 100 years to deplete the same amount of carbon.

(b) The chemical potential of carbon was not a linear function of composition in the functionally graded transition between the ferritic and austenitic alloys. The variation of chemical potential of carbon with distance indicates that no benefits are gained in compositional grading after 70% 800H, because further changes in composition cause no appreciable changes in the driving force for carbon diffusion.

(c) The microstructure of the compositionally graded joints changed gradually from martensitic near the build plate to a fully austenitic structure near the top sample. Since the austenite region does not provide any significant resistance to carbon diffusion, a shorter transition joint can be effectively used to achieve the same intended retardation of carbon diffusion.

(d) The accelerated heat treatment experiments at elevated temperature were designed to simulate service conditions for the dissimilar weld and graded joint. The functionally graded joints significantly performed the dissimilar weld in retarding carbon diffusion under service conditions as the carbon concentration profile remained virtually unchanged.

**Table 2**
Comparison of average computed carbon diffusion fluxes (mol/m$^2$-s) and depletion in the ferritic steel at different service times at 773 K in dissimilar joints between 2.25Cr-1Mo steel and Alloy 800H.

| Type of joint | | Number of years | | | | | |
|---|---|---|---|---|---|---|---|
| | | 2 | 5 | 10 | 20 | 50 | 100 |
| 2.25Cr-1Mo Steel / IN82 / Alloy 800H | Avg. Flux (x10$^{-13}$) | 1.97 | 4.94 | 9.87 | 19.6 | 15.2 | 7.85 |
| | Depletion | 2.0% | 5.0% | 10% | 20% | 23% | 29% |
| 2.25Cr-1Mo Steel / 10-100% 800H Gradient / Alloy 800H | Avg. Flux (x10$^{-13}$) | 0.157 | 0.392 | 0.785 | 1.57 | 3.92 | 7.85 |
| | Depletion | 0.12% | 0.3% | 0.6% | 1.2% | 3.1% | 5.0% |
| 2.25Cr-1Mo Steel / 10-70% 800H Gradient / Alloy 800H | Avg. Flux (x10$^{-13}$) | 0.157 | 0.392 | 0.785 | 1.57 | 3.92 | 7.85 |
| | Depletion | 0.12% | 0.3% | 0.6% | 1.2% | 3.1% | 5.0% |

## Acknowledgements

## References

[1] D. Roberts, R. Ryder, R. Viswanathan, Performance of dissimilar welds in service, J. Press. Ves. 107 (3) (1985) 247–254, https://doi.org/10.1115/1.3264443.

[2] C. Lundin, Dissimilar metal welds-transition joints literature review, Weld. J. 61 (2) (1982) 58–63.

[3] J. DuPont, R. Mizia, Review of Dissimilar Metal Welding for the NGNP Helical-coil Steam Generator, Idaho National Laboratory (INL), Idaho Falls, ID, 2010.

[4] J. DuPont, Microstructural evolution and high temperature failure of ferritic to austenitic dissimilar welds, Int. Mater. Rev. 57 (4) (2012) 208–234. https://doi.org/10.1179/1743280412Y.0000000006.

[5] M. Sireesha, V. Shankar, S.K. Albert, S. Sundaresan, Microstructural features of dissimilar welds between 316LN austenitic stainless steel and alloy 800, Mater. Sci. Eng. A 292 (1) (2000) 74–82. https://doi.org/10.1016/S0921-5093(00)00969-2.

[6] C. Jang, J. Lee, J.S. Kim, T.E. Jin, Mechanical property variation within Inconel 82/182 dissimilar metal weld between low alloy steel and 316 stainless steel, Int. J. Pres. Ves. Pip. 85 (9) (2008) 635–646. https://doi.org/10.1016/j.ijpvp.2007.08.004.

[7] J. Race, H. Bhadeshia, Precipitation sequences during carburisation of Cr–Mo steel, Mater. Sci. Tech. 8 (10) (1992) 875–882. https://doi.org/10.1179/mst.1992.8.10.875.

[8] G. Brentrup, B. Snowden, J. DuPont, J. Grenestedt, Design considerations of graded transition joints for welding dissimilar alloys, Weld. J. 91 (2012) 252–259.

[9] H. Wang, G. Wang, F. Xuan, S. Tu, Fracture mechanism of a dissimilar metal welded joint in nuclear power plant, Eng. Fail. Anal. 28 (2013) 134–148. https://doi.org/10.1016/j.engfailanal.2012.10.005.

[10] K. Laha, K. Chandravathi, K.B.S. Rao, S. Mannan, D. Sastry, An assessment of creep deformation and fracture behavior of 2.25 Cr-1Mo similar and dissimilar weld joints, Metall. Mater. Trans. A 32 (1) (2001) 115–124. https://doi.org/10.1007/s11661-001-0107-9.

[11] K. Laha, K.B.S. Rao, S. Mannan, Creep behaviour of post-weld heat-treated 2.25 Cr-1Mo ferritic steel base, weld metal and weldments, Mater. Sci. Eng. A 129 (2) (1990) 183–195. https://doi.org/10.1016/0921-5093(90)90265-5.

[12] R.M. Mahamood, E.T. Akinlabi, M. Shukla, S. Pityana, Functionally graded material: an overview, in: Proceedings of the World Congress on Engineering, London, UK, 2012, pp. 2–6.

[13] S. Kapuria, M. Bhattacharyya, A. Kumar, Bending and free vibration response of layered functionally graded beams: a theoretical model and its experimental validation, Compos. Struct. 82 (3) (2008) 390–402. https://doi.org/10.1016/j.compstruct.2007.01.019.

[14] Z.H. Melgarejo, O.M. Suárez, K. Sridharan, Wear resistance of a functionally-graded aluminum matrix composite, Scripta Mater. 55 (1) (2006) 95–98. https://doi.org/10.1016/j.scriptamat.2006.03.031.

[15] B.V. Krishna, W. Xue, S. Bose, A. Bandyopadhyay, Functionally graded Co–Cr–Mo coating on Ti–6Al–4V alloy structures, Acta Biomater. 4 (3) (2008) 697–706. https://doi.org/10.1016/j.actbio.2007.10.005.

[16] A. Bandyopadhyay, B. Krishna, W. Xue, S. Bose, Application of laser engineered net shaping (LENS) to manufacture porous and functionally graded structures for load bearing implants, J. Mater. Sci Mater. M. 20 (2009) 29–34. https://doi.org/10.1007/s10856-008-3478-2.

[17] G. Brentrup, J. DuPont, Fabrication and characterization of graded transition joints for welding dissimilar alloys, Weld. J. 92 (2013) 72–79.

[18] B.E. Carroll, R.A. Otis, J.P. Borgonia, J.-o. Suh, R.P. Dillon, A.A. Shapiro, D.C. Hofmann, Z.-K. Liu, A.M. Beese, Functionally graded material of 304L stainless steel and inconel 625 fabricated by directed energy deposition: characterization and thermodynamic modeling, Acta Mater. 108 (2016) 46–54. https://doi.org/10.1016/j.actamat.2016.02.019.

[19] L. Murr, S. Gaytan, F. Medina, H. Lopez, E. Martinez, B. Machado, D. Hernandez, L. Martinez, M. Lopez, R. Wicker, Next-generation biomedical implants using additive manufacturing of complex, cellular and functional mesh arrays, Philos. T. Roy. Soc. A 368 (1917) (2010) 1999–2032, https://doi.org/10.1098/rsta.2010.0010.

[20] R. Dehoff, M. Kirka, W. Sames, H. Bilheux, A. Tremsin, L. Lowe, S. Babu, Site specific control of crystallographic grain orientation through electron beam additive manufacturing, Mater. Sci. Tech. 31 (8) (2015) 931–938. https://doi.org/10.1179/1743284714Y.0000000734.

[21] D.C. Hofmann, S. Roberts, R. Otis, J. Kolodziejska, R.P. Dillon, J.-o. Suh, A.A. Shapiro, Z.-K. Liu, J.-P. Borgonia, Developing gradient metal alloys through radial deposition additive manufacturing, Sci. Rep. 4 (2014) 5357. https://doi.org/10.1038/srep05357.

[22] T. DebRoy, H. Wei, J. Zuback, T. Mukherjee, J. Elmer, J. Milewski, A. Beese, A. Wilson-Heid, A. De, W. Zhang, Additive manufacturing of metallic components–process, structure and properties, Prog. Mater. Sci. 92 (2018) 112–224. https://doi.org/10.1016/j.pmatsci.2017.10.001.

[23] U. Savitha, G.J. Reddy, A. Venkataramana, A.S. Rao, A. Gokhale, M. Sundararaman, Chemical analysis, structure and mechanical properties of discrete and compositionally graded SS316–IN625 dual materials, Mater. Sci. Eng. A 647 (2015) 344–352. https://doi.org/10.1016/j.msea.2015.09.001.

[24] C. Shen, Z. Pan, D. Cuiuri, J. Roberts, H. Li, Fabrication of Fe-FeAl functionally graded material using the wire-arc additive manufacturing process, Metall. Mater. Trans. B 47 (1) (2016) 763–772. https://doi.org/10.1007/s11663-015-0509-5.

[25] P. Muller, P. Mognol, J.-Y. Hascoet, Modeling and control of a direct laser powder deposition process for Functionally Graded Materials (FGM) parts manufacturing, J. Mater. Process. Technol. 213 (5) (2013) 685–692. https://doi.org/10.1016/j.jmatprotec.2012.11.020.

[26] M. Domack, J. Baughman, Development of nickel-titanium graded composition components, Rapid Prototyp. J. 11 (1) (2005) 41–51. https://doi.org/10.1108/13552540510573383.

[27] L.D. Bobbio, R.A. Otis, J.P. Borgonia, R.P. Dillon, A.A. Shapiro, Z.-K. Liu, A.M. Beese, Additive manufacturing of a functionally graded material from Ti-6Al-4V to Invar: experimental characterization and thermodynamic calculations, Acta Mater. 127 (2017) 133–142. https://doi.org/10.1016/j.actamat.2016.12.070.

[28] P. Collins, R. Banerjee, S. Banerjee, H. Fraser, Laser deposition of compositionally graded titanium–vanadium and titanium–molybdenum alloys, Mater. Sci. Eng. A 352 (1) (2003) 118–128. https://doi.org/10.1016/S0921-5093(02)00909-7.

[29] Z. Khayat, T. Palmer, Impact of iron composition on the properties of an additively manufactured solid solution strengthened nickel base alloy, Mater. Sci. Eng., A 718 (2018) 123–134. https://doi.org/10.1016/j.msea.2018.01.112.

[30] J.S. Keist, T.A. Palmer, Role of geometry on properties of additively manufactured Ti-6Al-4V structures fabricated using laser based directed energy deposition, Mater. Des. 106 (2016) 482–494. https://doi.org/10.1016/j.matdes.2016.05.045.

[31] E.R. Denlinger, J.C. Heigel, P. Michaleris, T. Palmer, Effect of inter-layer dwell time on distortion and residual stress in additive manufacturing of titanium and nickel alloys, J. Mater. Process. Technol. 215 (2015) 123–131. https://doi.org/10.1016/j.jmatprotec.2014.07.030.

[32] N. Saunders, A.P. Miodownik, CALPHAD (calculation of Phase Diagrams): a Comprehensive Guide, Elsevier, 1998.

[33] J.N. DuPont, J.C. Lippold, S.D. Kiser, Welding Metallurgy and Weldability of Nickel-base Alloys, John Wiley & Sons, Hoboken, NJ, 2009.

[34] A. Schaeffler, Constitution diagram for stainless steel weld metal, Metal Prog. 56 (11) (1949) 680.

[35] G. Ghosh, G. Olson, Computational thermodynamics and the kinetics of martensitic transformation, J. Phase Equil. 22 (3) (2001) 199. https://doi.org/10.1361/105497101770338653.

[36] A. Elrefaey, Y. Javadi, J.A. Francis, M.D. Callaghan, A.J. Leonard, Evolution of microstructure and toughness in 2.25 Cr-1Mo steel welds, Int. J. Pres. Ves. Pip. (2018). https://doi.org/10.1016/j.ijpvp.2018.05.006.

[37] P. Mayr, C. Schlacher, J.A. Siefert, J.D. Parker, Microstructural features, mechanical properties and high temperature failures of ferritic to ferritic dissimilar welds, Int. Mater. Rev. (2018) 1–26. https://doi.org/10.1080/09506608.2017.1410943.

[38] T. Mukherjee, J. Zuback, W. Zhang, T. DebRoy, Residual stresses and distortion in additively manufactured compositionally graded and dissimilar joints, Comput. Mater. Sci. 143 (2018) 325–337. https://doi.org/10.1016/j.commatsci.2017.11.026.

[39] R. Klueh, A. Nelson, Ferritic/martensitic steels for next-generation reactors, J. Nucl. Mater. 371 (1) (2007) 37–52. https://doi.org/10.1016/j.jnucmat.2007.05.005.